RSC Advances

PAPER

View Article Online
View Journal | View Issue

Cite this: *RSC Adv.*, 2023, **13**, 28767

Bacteria-derived topologies of Cu_2O nanozymes exert a variable antibacterial effect†

Ashish Kumar Shukla, *[a] Vinod Morya[a] and Bhaskar Datta *[ab]

Received 10th August 2023
Accepted 22nd September 2023

DOI: 10.1039/d3ra05411j

rsc.li/rsc-advances

The ability of bacteria to facilitate fabrication of nanomaterials has been adapted towards bacterial sensing applications. In this work, we fabricate spherical, cubic and truncated octahedron topologies of Cu_2O nanoparticles *via E. coli*-facilitated redox reaction in an electrochemical setup. The Cu_2O nanoparticles exhibit cytochrome c oxidase-like activity with the spherical topology displaying higher catalytic rate compared to the other geometries. The topology-dependent catalytic behavior of Cu_2O nanoparticles has not been reported previously. The Cu_2O nanozymes also display *E. coli* killing activity in a topology-correlated manner. The *E. coli* mediated redox reaction in an electrochemical setup is being reported for the first time for synthesis of different topologies of Cu_2O which also exert a variable antibacterial effect.

Introduction

Nanozymes have emerged as a unique class of nanomaterials due to their biocompatibility, affordability, and distinctive catalytic properties.[1–4] These synthetic nanomaterials imitate the activity of enzymes and find applications in therapeutics,[5,6] biosensors,[7–10] and for environmental remediation.[11–13] The fabrication of nanozymes[14,15] has been reported previously through various methods,[16–19] including biosynthesis,[20] electrochemical synthesis,[21] and wet chemical methods.[14,22] The rich biochemical and electrochemical capabilities of bacteria have been leveraged for fabrication of distinct morphologies of nanoparticles.[23,24] The chemical and physical properties associated with specific bacterial strains can affect the size and shape of nanoparticles being produced and which would suit specific applications.[17] The bacteria-mediated synthesis of nanomaterials is purported to render unique properties that are difficult to achieve with conventional fabrication techniques. Bacteria-facilitated synthesis of metal nanomaterials involves reduction of metal ions by characteristic reducing agents associated with the bacterial strain.[25] Previously, bacteria-mediated nanoparticle growth has been reported using various reducing agents such as enzymes (nitrate reductase[26] and hydrogenase[27]) and NADH- and NADH dependent enzyme cofactors.[28] These agents and cofactors provide the necessary reducing power, enabling the transformation of metal ions into nanoparticles. Understanding the diverse range of reducing agents and cofactors involved in bacteria-mediated nanoparticle growth is crucial for harnessing the full potential of this biosynthesis approach. Specifically, cupric reductase NDH-2 is associated with the surface of *E. coli* and has been utilized for the reduction of Cu^{2+} to Cu^{+}.[29] In this process, bacteria play a pivotal role in reducing metal ions to their metallic forms, leading to the formation of nanoparticles with unique properties. The ability of bacteria to drive topological diversity in nanomaterials is worthy of deeper scrutiny. Different morphologies of nanomaterials can significantly affect their chemical reactivity due to inherent differences in arrangement of atoms, bonding, and surface energy.[30] While nanoparticles with highly reactive surfaces are desirable, they are challenging to produce. Surfaces with high reactivity usually possess high surface energy, leading to rapid shrinkage during nanoparticle growth. The bacteria-derived biosynthesis of nanozymes continues to be explored in the context of different metal oxides and composites. While such synthesis relies on the ability of bacteria to catalyse formation of nanomaterials of uniform size and shape, the process is complex with multiple parameters that need to be optimized.

In this work, we synthesized spherical, cubic and truncated octahedron of cupric oxide (Cu_2O) nanozyme *via* a bacteria-mediated redox reaction in an electrochemical setup. The Cu_2O nanozyme displayed cytochrome c oxidase (CcO)-like activity with topology playing an unambiguous role in the catalytic activity of the nanozyme. Further, the Cu_2O nanozymes demonstrated *E. coli* killing in a topology-dependant manner. While the bacterial-mediated synthesis of nanomaterials and antibacterial properties of nanomaterials have been studied previously, we have not found any reports that converge both activities. The bacteria-facilitated synthesis of different topologies of Cu_2O nanoparticles and the differences in their cognate antibacterial activities suggests a distinctive and hitherto less explored combination of sensing and remediation.

[a]*Department of Biological Engineering, Indian Institute of Technology Gandhinagar, Gandhinagar 382055, India. E-mail: ashish.shukla@iitgn.ac.in*

[b]*Department of Chemistry, Indian Institute of Technology Gandhinagar, Gandhinagar 382055, India. E-mail: bdatta@iitgn.ac.in*

† Electronic supplementary information (ESI) available. See DOI: https://doi.org/10.1039/d3ra05411j

Results and discussion

The synthesis of distinct morphologies of the Cu_2O NPs were carried out by a bacteria-mediated redox reaction in an electrochemical setup. Previously, a variety of the electrochemical methods have been deployed for the synthesis of the different metal nanoparticles using three-electrode electrochemical setups.[31–33] In our experiments we also used three-electrode system for cyclic voltammetry study which include a CuO thin film on FTO substrate as a working electrode (WE), platinum (Pt) as a counter, and Ag/AgCl as a reference electrode. The CuO thin film was synthesized by modification of our previously reported method.[29] Characterization was performed by a combination of FESEM and XRD (see ESI†). In order to assess the bacteria-mediated redox processes at the CuO thin film, cyclic voltammetry was performed in the absence and presence of bacteria (1×10^4 CFU mL^{-1} DH-Alpha), in 30 mM KNO_3 electrolyte solution. The electrode was swept cathodically to reduce the CuO nanoparticles to Cu_2O nanoparticles, prospectively facilitated in the presence of bacteria. Based on the reductive changes being observed in the absence of bacteria, CuO nanoparticles present on the electrode surface are undergoing a two-electron reduction (Cu(II) to Cu(0)). In contrast, the presence of bacteria appears to facilitate a one-electron reduction of CuO nanoparticles (Cu(II) to Cu(I)) (Fig. 1A). The presence of cupric reductase NDH-2 on *E. coli* surface has been previously suggested to promote direct one-electron transfer from Cu(II) to Cu(I).[29] Specifically, when bacteria come in contact with a CuO electrode, it triggers a redox reaction (*E. coli* + Cu^{2+} + e^- → *E. coli* + Cu^+) at electrode surface. This reaction involves the reduction of copper oxide nanoparticles (CuO NPs) to cupric oxide nanoparticles (Cu_2O NPs), facilitated by cupric reductase NDH-2 enzyme present on the surface of the bacteria. Notably, a prominent oxidative peak is observed in the absence of bacteria that corresponds to the stripping of Cu(0) formed during the direct two-electron reduction.[34] The oxidative peak is significantly lower intensity in presence of bacteria, suggesting the reduction of Cu(II) to Cu(I) and concomitant formation of Cu_2O nanostructures on the surface of the WE. After the redox-reaction the surface of the FTO electrode clearly shows a brick-colored deposition following the reduction of CuO NPs to Cu_2O NPs in the presence of bacteria (see ESI†).

Based on our initial observations pertaining to the bacteria-facilitated synthesis of Cu_2O nanostructures, we hypothesized that provision of different reaction times at the electrode surface could influence the topology of Cu_2O nanostructures. In previous reports, topology-controlled platinum[35] and gold nanoparticles[36,37] were synthesized through electrochemical methods by manipulating the redox reaction time.[38] Accordingly, we performed different cycles of voltammetry response in the presence of bacteria. After 10 CV cycles of the redox reaction at the surface of the CuO electrode, we observed the formation of spherical Cu_2O nanoparticles. The morphology and size of Cu_2O nanoparticles changed upon further increase of CV cycles, with cubic structures being observed after 20 cycles and truncated octahedron after 30 cycles (Fig. 1B).

Similar structures of Cu_2O nanoparticles have been synthesized previously using wet chemical methods.[39,40] However, the bacteria-facilitated topological transformation of Cu_2O NPs in has not been reported previously. While such topologies of gold nanoparticles have been reported in the presence of bacteria,[41] to the best of our knowledge bacteria-facilitated growth of different topologies of metal oxide nanoparticles has not been reported. The different topologies of Cu_2O NPs obtained after 10, 20 and 30 CV cycles were characterized by FESEM (Fig. 2A–F).

The synthesis of the truncated octahedral Cu_2O nanostructures was further confirmed by energy dispersive X-ray (EDAX) elemental mappings of Fig. 2F, where copper, tin, oxygen and fluorine ions were evenly distributed on the FTO

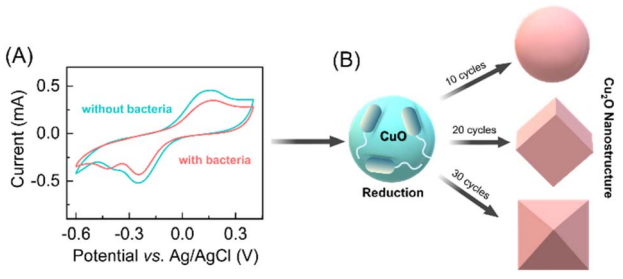

Fig. 1 (A) Cyclic voltagrams of a CuO thin film electrode in 30 mM KNO_3 solutions in the presence and absence of bacteria. (B) Bacteria-mediated reduction of CuO nanoparticles into different morphologies of Cu_2O nanostructures at different CV cycles (10, 20, and 30) with a scan rate of 40 mV s^{-1}.

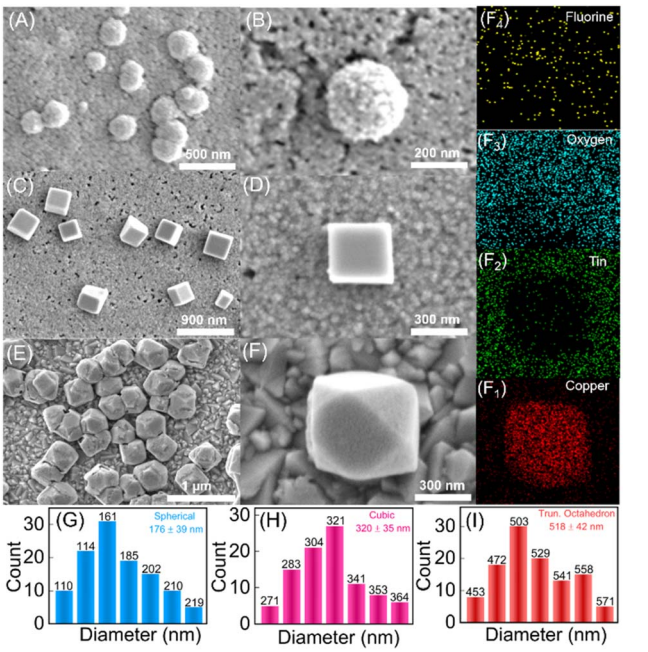

Fig. 2 Bacteria-mediated surface morphologies of Cu_2O nanoparticles. (A and B), (C and D) and (E and F) are the FESEM images of spherical, cubic and truncated octahedrons Cu_2O NPs. (F_1), (F_2), (F_3) and (F_4) show the EDAX spectra of corresponding elemental maps of image (F). Images (G), (H) and (I) show the particle distribution of the spherical, cubic and truncated octahedron Cu_2O NPs with an average diameter (176 ± 39), (320 ± 25), and (518 ± 42) nm, respectively.

substrate after performing the redox reaction (Fig. 2(F_1–F_4)). The spherical, cubic and truncated octahedron Cu_2O NPs display progressively greater sizes and broader size distributions with mean diameters of 176 nm, 320 nm and 518 nm, respectively as shown in Fig. 2G–I. Previously reported spherical Cu_2O nanoparticles were observed with mean diameter spanning 100–500 nm.[42,43] Cubic Cu_2O nanoparticles were found to possess sizes in the range of 400–600 nm[39,40] while truncated octahedron have been reported with singular methods of synthesis in the size range of 500–700 nm.[44] As one would intuitively expect, the formation of truncated octahedra is deeply connected to precursor concentrations, temperature, reaction time, and presence of additives. Nevertheless, the precise conditions and parameters underlying the growth of different topologies of Cu_2O NPs themselves vary across different reports.[45] In our experiments, the topologies of Cu_2O NPs obtained after 10, 20 and 30 cycles were found to be most uniform upon comparing results from variable number of CV cycles (ESI Fig. S4†).

The Cu_2O NPs produced after 10, 20 and 30 CV cycles were further analyzed by XRD. As shown in Fig. 3A, the characteristic diffraction peak 2θ of the fresh CuO thin film electrode appears at 35.56°, 38.8°, and 68.03° in the diffraction pattern. These correspond to reference card numbers 00-041-0254 (see ESI†). The XRD spectra of synthesized Cu_2O NPs with different morphologies on the FTO working electrode showed the characteristic FTO and Cu_2O peaks after the bacteria-mediated redox reaction. XRD spectra of Cu_2O NPs produced in presence of bacteria showed significant diffraction peak 2θ at 36.4°, 42.36°, and 73.63° for all (spherical, cubic and truncated octahedron) topologies. These match with reference card numbers 01-071-3645. In addition, FTIR spectra were also recorded for the different topologies of Cu_2O NPs. As shown in Fig. 3B, the O–H, C=C and C–O bond stretching vibrations at *ca.* 3300, 1647 and 907 cm^{-1}, respectively, become more prominent. These changes confirm the composition and bonding of the Cu_2O NPs across all the observed topologies.[46,47]

The change in oxidation state of the Cu was further validated through X-ray photoelectron spectroscopy (XPS) studies. The survey scan of the electrodes before and after the redox reaction were performed which contains peaks characteristic of Cu 2p,

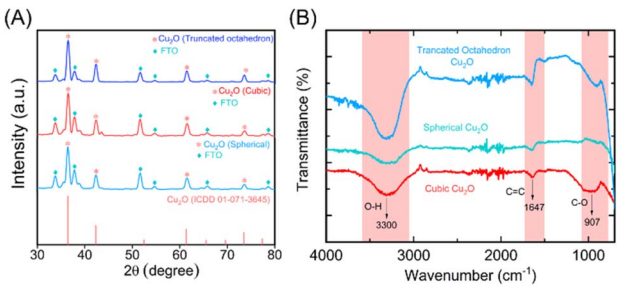

Fig. 3 (A) XRD spectra of the CuO thin film electrode after bacteria-mediated redox reaction at different CV cycles (10, 20, and 30). The formation of Cu_2O NPs over the electrode surface can be seen clearly in the XRD spectra at different CV cycles. Image (B) shows the FTIR spectra of different morphologies of Cu_2O NPs.

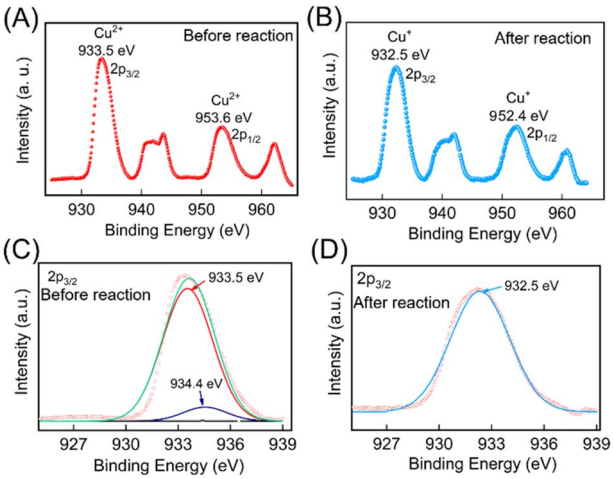

Fig. 4 Scan XPS spectra before (A) and (B) after redox reaction recorded within specific binding energy ranges (925 to 970 eV). (C) and (D) show the presence of Cu^{2+} and Cu^{+} ions at 933.5 eV and 932.5 eV binding energy values, respectively.

and O 1s (ESI Fig. S5†). To further confirm the oxidation states of Cu pre- and post-redox reaction, narrow scan XPS spectra were recorded within the BE ranges (925 to 970 eV) and are depicted in Fig. 4A and B. The data were deconvoluted using Fityk software, which identified the presence of two oxidation states of Cu. These peak positions were cross-referenced with the NIST XPS database to identify the oxidation states of the Cu ion. Before the redox reaction, the peaks at BE values 933.5 eV and 934.4 eV in the narrow scan spectra for Cu 2P (Fig. 4C) closely matched the BE of $2P_{3/2}$ states of Cu^{2+}. After the redox reaction, a peak at BE values 932.5 eV in the narrow scan spectra for Cu 2P (as depicted in Fig. 4D) closely aligned with the BE of $2P_{3/2}$ states of Cu^{+}, thereby confirming the formation of Cu_2O NPs. The complete details of the XPS analysis are provided in the ESI.†

Cytochrome c oxidase (CcO)-like activity of the Cu_2O nanoparticles

Cu_2O NPs demonstrate reversible redox behavior involving Cu^{+} and Cu^{2+} species, like enzyme-catalyzed redox reactions. We expected the different topologies of Cu_2O NPs to not only mimic cytochrome c oxidase (CcO) enzyme activity, but also display topology-dependent behavior as nanozymes owing to the distinctive structural attributes of each geometry.[48] By precisely controlling the shape and size of Cu_2O NPs during synthesis, their catalytic performance can be optimized, potentially distinguishing their enzyme-like activity. Therefore, we studied the CcO enzyme-like behavior of the three topologies of the Cu_2O NPs against the cytochrome c (Cyt c) substrate. Natural CcO enzyme accepts electrons from the ferrous Cyt c and reduces oxygen O_2 to H_2O. The UV spectrum of oxidized Cyt c shows absorption peaks at 408 and 530 nm, while reduced Cyt c has absorption peaks at 414, 512 and 550 nm.[48] We used the peak at 550 nm to monitor and quantify the amount of reduced Cyt c. We first prepared ferrous Cyt c as per details provided in ESI.†

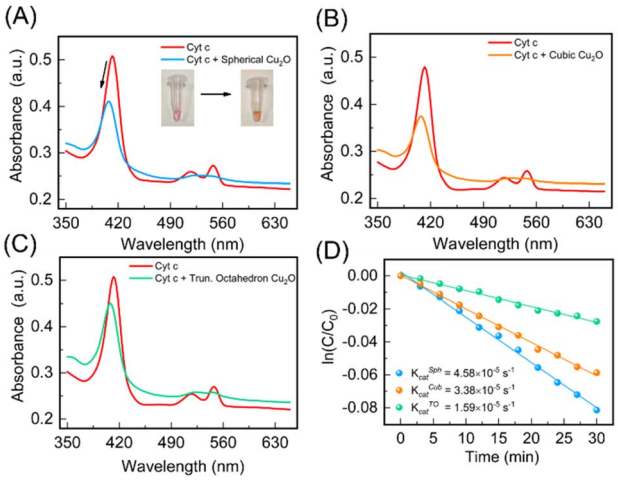

Fig. 5 The catalytic activity of different morphologies of the Cu_2O nanoparticles. (A) Spherical (B) cubic (C) truncated octahedron. Image (D) shows the kinetic reduction of the ferrous Cyt c at 550 nm for all morphologies of Cu_2O NPs for a period of 30 min. Inset: A change in color of the solution was observed when ferrous Cyt c converted into ferric Cyt c.

The scrub Cu_2O NPs were taken out from the FTO substrate in powder form. The physical appearance of the Cu_2O NPs obtained after 10, 20 and 30 CV cycles are shown in ESI (Fig. S4†). Upon addition of a 1 mg mL^{-1} solution of Cu_2O nanoparticles, the absorbance peak of 10 μM of ferrous Cyt c at 414 nm shifted to 408 nm. However, the absorbance peak at 550 nm gradually decreased confirming the catalytic activity of Cu_2O NPs (see Fig. 5A). In addition, the color of the Cyt c solution changed from pink to a yellowish red (Fig. 5A, inset), suggesting the conversion of Cyt c from ferrous to ferric form. This conversion is further confirmed by circular dichroism (CD) spectroscopy (see ESI†) and consistent with the previous reports.[48]

The cubic and truncated octahedron topologies of Cu_2O NPs displayed an analogous reduction of ferrous Cyt c to ferric Cyt c (Fig. 5B and C). The catalytic activity of the different topologies of Cu_2O NPs were quantified by studying the time-resolved reduction of ferrous Cyt c. The absorbance at 550 nm for each of the spherical, cubic and truncated octahedral Cu_2O NPs was measured over time (Fig. 5D). The catalytic rate constants of the spherical (K_{cat}^{Sph}), cubic (K_{cat}^{Cub}) and truncated octahedron (K_{cat}^{TO}) are found to be 4.58×10^{-5} s^{-1}, 3.38×10^{-5} s^{-1} and 1.59×10^{-5} s^{-1}. These rate constants are consistent with previously reported catalytic rates.[48] Our measurements indicate that the oxidation of ferrous Cyt c with cubic and truncated octahedron NPs is slower compared to spherical NPs. This observation aligns with the intuitive expectation that smaller particle sizes are likely to exert higher catalytic activity.[49] Smaller nanoparticles have a higher surface-to-volume ratio, providing more active sites for catalytic reactions. Also, increased density of surface atoms and exposure of reactive sites enhance catalytic efficiency. Additionally, smaller nanoparticles offer shorter diffusion distances enabling faster mass transport and more efficient interaction between reactants and the catalyst, leading to increased reaction rates.

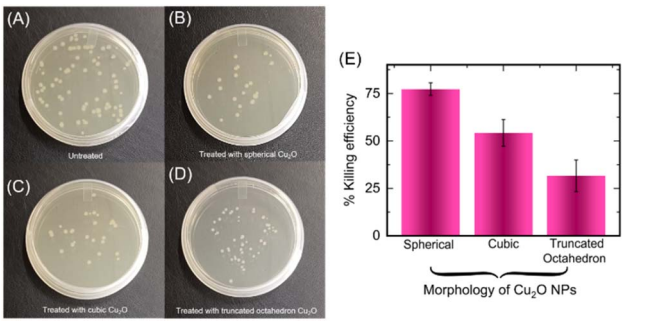

Fig. 6 The antibacterial effect of the different morphologies of the Cu_2O nanoparticles where (A) shows the untreated growth of the *E. coli* (DH5-Alpha) bacteria. Images (B), (C) and (D) show treated growth profiles of *E. coli* (DH-Alpha) bacteria after 15 min of incubation with spherical, cubic and truncated octahedron Cu_2O NPs, respectively. Image (E) shows the killing efficiency of the synthesized different morphologies Cu_2O nanoparticles.

Cuprous oxide has the ability to disrupt various cell functions and can be toxic to cells, making it a promising agent for inhibiting microbial growth.[50–52] These nanoparticles can also damage microbial components through various mechanisms such as generation of reactive oxygen species (ROS),[53] disruption of cell walls/membranes,[54] replacement of native cofactors in metalloproteins[55,56] and damage of intracellular components.[57] The fabrication of different topologies of copper-containing nanoparticles has been considered for tuning antibacterial effect and enabling broad scope of use in environmental remediation.[58] Notably, octahedral and cubic-shaped Cu_2O nanoparticles have been used to target specific pollutants and allow for greater control over their activity.[59] We were interested in studying antibacterial activity of the different topologies of Cu_2O NPs that were produced *via* bacteria-mediated electrochemical approach. Accordingly, we incubated the spherical, cubic and truncated octahedron of Cu_2O NPs (1 mg mL^{-1}) with *E. coli* bacteria. Interestingly, *E. coli* are inhibited in presence of all the topologies of Cu_2O NPs albeit with different efficiencies (Fig. 6A–D).

The percentage killing efficiency due to spherical, cubic and truncated octahedron nanoparticles were found to be 77%, 54%, and 31%, respectively (Fig. 6D).[60] The differing inhibitory effects of the three topologies of Cu_2O NPs against *E. coli* is consistent with previous reports.[59,61] The spherical Cu_2O NPs display substantially higher antibacterial effect potentially due to smaller size and higher surface area-to-volume ratios, which likely permit better interaction with bacterial cells compared to the other topologies. Two mechanisms of antibacterial activity are likely at play for the Cu_2O NPs. Also, as mentioned above, Cu_2O NPs are capable of generating reactive oxygen species (ROS) that can cause damage to cellular constituents.[62,63] The source of energy for ROS production in our setup is primarily through Fenton type and Haber–Weiss reactions given as below.[51]

$$Cu^{+} + O_2 \rightarrow Cu^{2+} + O_2^{\cdot -}$$

$$2O_2^{\bullet -} + 2H^+ \rightarrow H_2O_2 + O_2$$

$$Cu^+ + H_2O_2 \rightarrow Cu^{2+} + OH^{\bullet} + OH^-$$

The unique morphology and surface characteristics of the Cu_2O NPs can facilitate redox reactions at the particle–cell interface leading to ROS production, without the need for external energy sources like light, electronic energy, or heat.[64–66] Cu_2O NPs can also produce disruptions in microbial cell wall and cell membrane thereby exerting bactericidal effects.[50]

Conclusions

In summary, we have used a bacteria-facilitated redox technique to fabricate different morphologies of the cytochrome c oxidase (CcO)-mimic Cu_2O nanozyme and demonstrated their antibacterial effect. The Cu_2O NPs were prepared by a hitherto unreported bacteria-mediated redox reaction in an electrochemical setup and involved preferential reduction (Cu(II) to Cu(I)) of the CuO thin film electrode during cyclic voltammetry. The morphologies and size of the Cu_2O NPs, depend upon the redox reaction time at the surface of the electrode during CV measurements. After 10, 20, and 30 cycles of CV study, we observed spherical, cubic and truncated octahedron morphologies of the Cu_2O nanoparticles, respectively. The catalytic activity of the different morphology of the nanoparticles was calculated against Cyt c substrate and spherical Cu_2O NPs showed superior catalytic activity compared to the other two topologies. While all the topologies of Cu_2O NPs displayed antibacterial activity against *E. coli* (DH5-Alpha strain), spherical Cu_2O NPs showed highest bacterial killing efficiency compared to the other Cu_2O NP topologies. For future prospects, our study suggests the exploration of a generalized approach for the synthesis of different topologies of nanozymes in response to bacteria with specific redox reaction, followed by evaluating the bacterial killing ability of these nanozymes. This methodology can be applied and tested with various types of nanoparticles thereby opening avenues for broader applications and innovative antimicrobial strategies.

Author contributions

A. K. S. and B. D. conceived the idea and planned the experiments. A. K. S. designed and performed most of the experiments. V. M. helped with the UV spectroscopy measurements. A. K. S. and B. D. analysed the data and wrote the final draft of the manuscript.

Conflicts of interest

There are no conflicts to declare.

Acknowledgements

The authors are grateful to IIT Gandhinagar for their financial support for this work. Dr Bhaskar Datta thanks to Gujarat Council of Science & Technology for GUJCOST support (project no. GUJCOST/STI/2023-24/254). We acknowledge the help received from Dr Chinmay Ghoroi and CRTDH lab for helping us with instruments (UV-vis spectroscopy and sonicator). We also acknowledge the help received from Dr Biswajit Mondal for helping us with Auto Lab instrument. We also thank the Central Instrument Facility (CIF) at Indian Institute of Technology Gandhinagar, India, for SEM, XRD and EDAX characterization of experimental samples.

References

1 H. Wei and E. Wang, *Chem. Soc. Rev.*, 2013, **42**, 6060–6093.
2 J. Wu, X. Wang, Q. Wang, Z. Lou, S. Li, Y. Zhu, L. Qin and H. Wei, *Chem. Soc. Rev.*, 2019, **48**, 1004–1076.
3 H. Wang, K. Wan and X. Shi, *Adv. Mater.*, 2019, **31**, e1805368.
4 Y. Zhou, B. Liu, R. Yang and J. Liu, *Bioconjugate Chem.*, 2017, **28**, 2903–2909.
5 D. Li, D. Dai, G. Xiong, S. Lan and C. Zhang, *Small*, 2023, **19**, e2205870.
6 X. Wang, Y. Hu and H. Wei, *Inorg. Chem. Front.*, 2016, **3**, 41–60.
7 M. Cai, Y. Zhang, Z. Cao, W. Lin and N. Lu, *ACS Appl. Mater. Interfaces*, 2023, **15**, 18620–18629.
8 Y. Wu, D. C. Darland and J. X. Zhao, *Sensors*, 2021, **21**, 5201.
9 W. Lu, Y. Guo, J. Zhang, Y. Yue, L. Fan, F. Li, C. Dong, S. Shuang and A. High, *ACS Appl. Mater. Interfaces*, 2022, **14**, 57206–57214.
10 A. K. Shukla, S. Bhandari and K. K. Dey, *Mater. Today Commun.*, 2021, **28**, 102504.
11 R. Singh, A. Umapathi, G. Patel, C. Patra, U. Malik, S. K. Bhargava and H. K. Daima, *Sci. Total Environ.*, 2022, **854**, 158771.
12 Y. Meng, W. Li, X. Pan and G. M. Gadd, *Environ. Sci.: Nano*, 2020, **7**, 1305–1318.
13 A. K. Shukla, D. Bhatia and K. K. Dey, *ACS Appl. Nano Mater.*, 2023, **6**, 8017–8027.
14 Y. Huang, J. Ren and X. Qu, *Chem. Rev.*, 2019, **119**, 4357–4412.
15 C. Ge, G. Fang, X. Shen, Y. Chong, W. G. Wamer, X. Gao, Z. Chai, C. Chen and J. J. Yin, *ACS Nano*, 2016, **10**, 10436–10445.
16 M. Eugenio, N. Müller, S. Frasés, R. Almeida-Paes, L. M. T. R. Lima, L. Lemgruber, M. Farina, W. de Souza and C. Sant'Anna, *RSC Adv.*, 2016, **6**, 9893–9904.
17 S. Ghosh, R. Ahmad, Md. Zeyaullah and S. K. Khare, *Front. Chem.*, 2021, **9**, 626834.
18 N. Shreyash, S. Bajpai, M. A. Khan, Y. Vijay, S. K. Tiwary and M. Sonker, *ACS Appl. Nano Mater.*, 2021, **4**, 11428–11457.
19 C. A. S. Ballesteros, L. A. Mercante, A. D. Alvarenga, M. H. M. Facure, R. Schneider and D. S. Correa, *Mater. Chem. Front.*, 2021, **5**, 7419–7451.
20 S. Nakamura, M. Sato, Y. Sato, N. Ando, T. Takayama, M. Fujita and M. Ishihara, *Int. J. Mol. Sci.*, 2019, **20**, 362.
21 M. A. Komkova, K. R. Vetoshev, E. A. Andreev and A. A. Karyakin, *Dalton Trans.*, 2021, **50**, 11385–11389.
22 H. Wang, K. Wan and X. Shi, *Adv. Mater.*, 2019, **31**, e1805368.

23 N. Goel, R. Ahmad, R. Singh, S. Sood and S. K. Khare, *Bioresour. Technol. Rep.*, 2021, **15**, 100753.
24 M. T. Yaraki, S. Zahed Nasab, I. Zare, M. Dahri, M. Moein Sadeghi, M. Koohi and Y. N. Tan, *Ind. Eng. Chem. Res.*, 2022, **61**, 7547–7593.
25 A. Ramesh, M. T. Sundari, and P. E. Thirugnanam, *Bio-Nanoparticles*, John Wiley & Sons, Ltd, 2015, pp. 53–81.
26 S. Anil Kumar, M. K. Abyaneh, S. W. Gosavi, S. K. Kulkarni, R. Pasricha, A. Ahmad and M. I. Khan, *Biotechnol. Lett.*, 2007, **29**, 439–445.
27 C. K. Ng, T. K. C. Cai Tan, H. Song and B. Cao, *RSC Adv.*, 2013, **3**, 22498–22503.
28 S. He, Z. Guo, Y. Zhang, S. Zhang, J. Wang and N. Gu, *Mater. Lett.*, 2007, **61**, 3984–3987.
29 A. K. Shukla, S. Mitra, S. Dhakar, A. Maiti, S. Sharma and K. K. Dey, *ACS Appl. Bio Mater.*, 2023, **6**, 117–125.
30 X. Wang, H. F. Wu, Q. Kuang, R. B. Huang, Z. X. Xie and L. S. Zheng, *Langmuir*, 2010, **26**, 2774–2778.
31 L. Rodríguez-Sánchez, M. C. Blanco and M. A. López-Quintela, *J. Phys. Chem. B*, 2000, **104**, 9683–9688.
32 Y. Gao and J. Hao, *J. Phys. Chem. B*, 2009, **113**, 9461–9471.
33 L. Jiang, I. Santiago and J. Foord, *Langmuir*, 2020, **36**, 6089–6094.
34 G. Zampardi, J. Thöming, H. Naatz, H. M. A. Amin, S. Pokhrel, L. Mädler and R. G. Compton, *Small*, 2018, **14**, e1801765.
35 L. Wei, Y.-J. Fan, H.-H. Wang, N. Tian, Z.-Y. Zhou and S.-G. Sun, *Electrochim. Acta*, 2012, **76**, 468–474.
36 D. Y. Kim, S. H. Im, O. O. Park and Y. T. Lim, *CrystEngComm*, 2010, **12**, 116–121.
37 M. H. Huang and P.-H. Lin, *Adv. Funct. Mater.*, 2012, **22**, 14–24.
38 L. Wei, N. Tian, Z. Y. Zhou and S. G. Sun, *Adv. Electrochem. Sci. Eng.*, 2017, 59–95.
39 Q. Hua, D. Shang, W. Zhang, K. Chen, S. Chang, Y. Ma, Z. Jiang, J. Yang and W. Huang, *Langmuir*, 2011, **27**, 665–671.
40 A. K. Mishra and D. Pradhan, *Cryst. Growth Des.*, 2016, **16**, 3688–3698.
41 M. Gericke and A. Pinches, *Hydrometallurgy*, 2006, **83**, 132–140.
42 S. Yadav, A. Jain and P. Malhotra, *Green Chem.*, 2019, **21**, 937–955.
43 M. A. Bhosale and B. M. Bhanage, *Adv. Powder Technol.*, 2016, **27**, 238–244.
44 J. Ouyang, H. Yang and A. Tang, *Mater. Des.*, 2016, **92**, 261–267.
45 S. S. Sawant, A. D. Bhagwat and C. M. Mahajan, *J. Nano-Electron. Phys.*, 2016, **8**, 01035.
46 S. Joshi, S. J. Ippolito and M. V. Sunkara, *RSC Adv.*, 2016, **6**, 43672–43684.
47 I. Roy, A. Bhattacharyya, G. Sarkar, N. R. Saha, D. Rana, P. P. Ghosh, M. Palit, A. R. Das and D. Chattopadhyay, *RSC Adv.*, 2014, **4**, 52044–52052.
48 M. Chen, Z. Wang, J. Shu, X. Jiang, W. Wang, Z. H. Shi and Y. W. Lin, *Inorg. Chem.*, 2017, **56**, 9400–9403.
49 P. Suchomel, L. Kvitek, R. Prucek, A. Panacek, A. Halder, S. Vajda and R. Zboril, *Sci. Rep.*, 2018, **8**, 4589.
50 K. Sunada, M. Minoshima and K. Hashimoto, *J. Hazard. Mater.*, 2012, **235–236**, 265–270.
51 X. Ma, S. Zhou, X. Xu and Q. Du, *Front. Surg.*, 2022, **9**, 905892.
52 N. Zhu, S. Zhou, J. Gong, X. Wang, C. Zhang, W. Li, D. Sheng, X. Liu, L. Xia and W. Xu, *Ind. Crops Prod.*, 2022, **187**, 115442.
53 M. R. Gunther, P. M. Hanna, R. P. Mason and M. S. Cohen, *Arch. Biochem. Biophys.*, 1995, **316**, 515–522.
54 D. Mitra, E. T. Kang and K. G. Neoh, *ACS Appl. Mater. Interfaces*, 2020, **12**, 21159–21182.
55 G. Tan, J. Yang, T. Li, J. Zhao, S. Sun, X. Li, C. Lin, J. Li, H. Zhou, J. Lyu and H. Ding, *Appl. Environ. Microbiol.*, 2017, **83**, e00867.
56 L. Macomber and J. A. Imlay, *Proc. Natl. Acad. Sci. U. S. A.*, 2009, **106**, 8344–8349.
57 A. K. Chatterjee, R. Chakraborty and T. Basu, *Nanotechnology*, 2014, **25**, 135101.
58 X. Zhu, J. Wang, L. Cai, Y. Wu, M. Ji, H. Jiang and J. Chen, *J. Hazard. Mater.*, 2022, **430**, 128436.
59 H. Pang, F. Gao and Q. Lu, *Chem. Commun.*, 2009, **9**, 1076–1078.
60 A. M. Ghadiri, N. Rabiee, M. Bagherzadeh, M. Kiani, Y. Fatahi, A. Di Bartolomeo, R. Dinarvand and T. J. Webster, *Nanotechnology*, 2020, **31**, 425101.
61 L. Xiong, H. Yu, C. Nie, Y. Xiao, Q. Zeng, G. Wang, B. Wang, H. Lv, Q. Li and S. Chen, *RSC Adv.*, 2017, **7**, 51822–51830.
62 R. L. Davies and S. F. Etris, *Catal. Today*, 1997, **36**, 107–114.
63 J. A. Imlay, *Annu. Rev. Microbiol.*, 2003, **57**, 395–418.
64 T. Xia, M. Kovochich, J. Brant, M. Hotze, J. Sempf, T. Oberley, C. Sioutas, J. I. Yeh, M. R. Wiesner and A. E. Nel, *Nano Lett.*, 2006, **6**, 1794–1807.
65 K. T. Kim, S. J. Klaine, J. Cho, S.-H. Kim and S. D. Kim, *Sci. Total Environ.*, 2010, **408**, 2268–2272.
66 E.-J. Park, J. Choi, Y.-K. Park and K. Park, *Toxicology*, 2008, **245**, 90–100.